

# Boosting Activity and Selectivity of CO<sub>2</sub> Electroreduction by Pre-Hydrizing Pd Nanocubes

Qiaowan Chang, Jeonghyeon Kim, Ji Hoon Lee, Shyam Kattel,\* Jingguang G. Chen,\* Sang-Il Choi,\* and Zheng Chen\*

The electrochemical CO<sub>2</sub> reduction reaction (CO<sub>2</sub>RR) to syngas represents a promising solution to mitigate CO<sub>2</sub> emissions and manufacture value-added chemicals. Palladium (Pd) has been identified as a potential candidate for syngas production via CO<sub>2</sub>RR due to its transformation to Pd hydride under CO<sub>2</sub>RR conditions, however, the pre-hydrized effect on the catalytic properties of Pd-based electrocatalysts has not been investigated. Herein, pre-hydrized Pd nanocubes (PdH<sub>0.40</sub>) supported on carbon black (PdH<sub>0.40</sub> NCs/C) are directly prepared from a chemical reduction method. Compared with Pd nanocubes (Pd NCs/C), PdH<sub>0.40</sub> NCs/C presented an enhanced CO<sub>2</sub>RR performance due to its less cathodic phase transformation revealed by the in situ X-ray absorption spectroscopy. Density functional theory calculations revealed different binding energies of key reaction intermediates on PdH<sub>0.40</sub> NCs/C and Pd NCs/C. Study of the size effect further suggests that NCs of smaller sizes show higher activity due to their more abundant active sites (edge and corner sites) for CO<sub>2</sub>RR. The pre-hydrization and reduced NC size together lead to significantly improved activity and selectivity of CO<sub>2</sub>RR.

from the utilization of fossil fuels.<sup>[1]</sup> The electrochemical CO<sub>2</sub> reduction reaction (CO<sub>2</sub>RR), combined with renewable energy sources (i.e., solar and wind), represents a promising solution.<sup>[2–5]</sup> In CO<sub>2</sub>RR, CO<sub>2</sub> can be converted into CO, hydrocarbons, or oxygenates. Since the reaction is generally performed under cathodic conditions in aqueous electrolyte, H<sub>2</sub> is inevitably produced as a byproduct from the competing hydrogen reduction reaction (HER). While significant efforts have been made on prohibiting HER by designing sophisticated electrocatalysts, electrodes, or cell structures, low selectivity toward CO<sub>2</sub>RR remains a critical challenge.<sup>[6–8]</sup> Instead of suppressing HER, combining the CO<sub>2</sub>RR and HER together has been considered as a viable approach, which produces syngas (CO and H<sub>2</sub>) with tunable CO/H<sub>2</sub> molar ratios that can be readily used to manufacture value-

added chemicals using exiting thermochemical processes, such as the Fischer–Tropsch and methanol synthesis reactions.<sup>[9–12]</sup>

Palladium (Pd) has been identified as a potential candidate for the production of syngas via CO<sub>2</sub>RR.<sup>[9,13–17]</sup> While Pd itself is a good HER catalyst, it was considered to be unsuitable for CO

## 1. Introduction

Efficient CO<sub>2</sub> storage and utilization technologies are urgently needed to mitigate the global climate change and ocean acidification issues caused by the continuing increase of CO<sub>2</sub> levels

Q. Chang, Prof. Z. Chen  
Department of NanoEngineering  
University of California San Diego  
La Jolla, CA 92093, USA  
E-mail: zhengchen@eng.ucsd.edu

Q. Chang, Prof. Z. Chen  
Program of Chemical Engineering  
University of California San Diego  
La Jolla, CA 92093, USA

J. Kim, Prof. S.-I. Choi  
Department of Chemistry and Green-Nano Materials Research Center  
Kyungpook National University  
Daegu 41566, Republic of Korea  
E-mail: sichoi@knu.ac.kr

Prof. J. H. Lee  
School of Materials Science and Engineering  
Kyungpook National University  
Daegu 41566, Republic of Korea

Prof. J. H. Lee, Prof. J. G. Chen  
Department of Chemical Engineering  
Columbia University  
New York, NY 10027, USA  
E-mail: jgchen@columbia.edu

Prof. S. Kattel  
Department of Physics  
Florida A&M University  
Tallahassee, FL 32307, USA  
E-mail: shyam.kattel@famu.edu

Prof. J. G. Chen  
Chemistry Division  
Brookhaven National Laboratory  
Upton, NY 11973, USA

Prof. Z. Chen  
Sustainable Power, and Energy Center  
University of California, San Diego  
La Jolla, CA 92093, USA

 The ORCID identification number(s) for the author(s) of this article can be found under <https://doi.org/10.1002/smll.202005305>.

DOI: 10.1002/smll.202005305

production in CO<sub>2</sub>RR due to its strong CO binding that leads to CO poisoning.<sup>[18]</sup> Sheng et al. revealed that Pd can be transformed into palladium hydride (PdH<sub>1</sub>) that presents decreased \*CO and \*H binding energies, which in turn adjusts the CO/H<sub>2</sub> ratios from the CO<sub>2</sub>RR and thus makes Pd a potential electrocatalyst for syngas production.<sup>[9]</sup> Moreover, the CO/H<sub>2</sub> ratio can be further improved by using Pd-based bimetallic catalysts and/or supporting Pd on metal carbides and nitrides.<sup>[11,13,19]</sup> The key to tune the CO/H<sub>2</sub> ratio over Pd-based electrocatalyst is to control the formation of the PdH<sub>1</sub> phase, specifically, the hydride formation potentials during the CO<sub>2</sub>RR. Lee et al. found that by alloying with first-row transition metals, the hydride formation potentials of PdM (M = Cu, Ni) were cathodically shifted, enabling the syngas production with the CO/H<sub>2</sub> ratios between 1 and 2 at 0.9 V (versus reversible hydrogen electrode or RHE).<sup>[13]</sup> In spite of these prior investigations, the electrocatalytic performance of PdH<sub>x</sub> has been rarely explored with different H contents, especially in a viewpoint of the structure–property–activity relationship. Moreover, it is not a trivial task to further enhance its CO<sub>2</sub>RR activity and tune the CO/H<sub>2</sub> ratio in a range of 1–2 (desired for the thermochemical processes) in the low overpotential range (between –0.5 and –0.7 V).<sup>[13,17]</sup>

In this work, we succeeded in overcoming the above challenges via a prehydridization process, using PdH<sub>0.40</sub> nanocubes supported on carbon black (PdH<sub>0.40</sub> NCs/C) that were directly prepared from a chemical reduction method to in situ elucidate the structure–property–activity relationship of PdH<sub>x</sub> during the CO<sub>2</sub>RR. The prehydridization process not only makes PdH<sub>0.40</sub> NCs/C readily for the in situ hydride phase transformation during CO<sub>2</sub>RR but also optimizes the hydride formation potentials. Compared with Pd nanocubes supported by carbon (Pd NCs/C), the CO/H<sub>2</sub> ratios and CO<sub>2</sub>RR activity of PdH<sub>0.40</sub> NCs/C with a similar size were enhanced by 77% and 220% at the low overpotential (i.e., –0.6 V), respectively. Moreover, to achieve a CO/H<sub>2</sub> ratio between 1 and 2, the suitable potential range for syngas production with 7 nm PdH<sub>0.40</sub> NCs/C catalyst was extended by 300 mV (from –0.5 to –0.8 V) compared with Pd NCs/C. In situ X-ray absorption fine structure (XAFS) analysis showed that the extended potential with more favorable CO/H<sub>2</sub> ratios for PdH<sub>0.40</sub> NCs/C was due to its less cathodic phase transformation to the stoichiometric PdH<sub>1</sub>. Density functional theory (DFT) calculations revealed that the binding energies of key CO<sub>2</sub>RR intermediates, such as \*HOCO and \*CO, were different on PdH<sub>0.40</sub> and Pd, leading to enhanced activity and selectivity on PdH<sub>0.40</sub>. We also found a strong size effect for both Pd and PdH<sub>0.40</sub> NCs/C, showing an increased CO/H<sub>2</sub> ratios with a smaller particle size. Our work demonstrates the critical role of the prehydridization over Pd-based electrocatalyst for CO<sub>2</sub>RR, opening up new directions for improving the activity and selectivity for syngas production.

## 2. Results and Discussion

PdH<sub>0.40</sub> NCs were obtained from the hydrogenation of as-prepared Pd NCs with the assistance of *N,N*-dimethylformamide (DMF) and polyvinyl pyrrolidone (PVP) (see the details in supporting information).<sup>[20]</sup> Transmission electron microscopy (TEM) images (Figure 1a,b) showed the well-controlled cubic

morphology of monodispersed Pd and PdH<sub>0.40</sub> NCs. After the hydrogenation conversion from Pd to PdH<sub>0.40</sub> NCs, the original Pd cubic morphology could be retained, indicated by the similar average edge length of Pd (71 ± 0.8 nm) and PdH<sub>0.40</sub> (73 ± 0.5 nm) NCs, and their high shape uniformity (>90%) (Figure S1, Supporting Information). The high-resolution TEM (HRTEM) images for an individual Pd and PdH<sub>0.40</sub> NC presented dominant Pd(200) facet exposed on both the NC surfaces (Figure 1c,d). Due to the insertion of H into the Pd lattice, the lattice spacing for the Pd(200) plane was increased from 1.94 Å (Pd NCs) to 1.99 Å (PdH<sub>0.40</sub> NCs) as shown in Figure 1e–f, in good agreement with the X-ray diffraction (XRD) results (Figure S2, Supporting Information). The elemental composition of PdH<sub>0.40</sub> NCs was determined by the linear relationship of lattice distance with hydrogen content<sup>[21]</sup> (Equation S1 and Table S1, Supporting Information). The XRD patterns showed no peak shift after storing PdH<sub>0.40</sub> NCs at room temperature in air even for 12 months (Figure S3, Supporting Information), indicating their good stability.<sup>[22]</sup>

The electronic structures of the Pd and PdH<sub>0.40</sub> NCs were revealed by the core-level and valence band spectra from X-ray photoelectron spectroscopy (XPS). Compared with Pd NCs, the Pd 3d core level spectrum of PdH<sub>0.40</sub> NCs was shifted to a higher binding energy (Figure S4a, Supporting Information), and its valence band spectrum presented a decreased bandwidth and emergence of two small shake-up peaks (marked as red arrows, Figure S4b, Supporting Information). These phenomena could be attributed to the reduction of the density of state near the Fermi level of PdH<sub>0.40</sub> relative to the Pd counterpart, specifically, the charge transfer between fully filled Pd 4d orbital and half-empty H 1s orbitals.<sup>[23–24]</sup> These XPS results confirmed the formation of Pd hydride associated with the charge transfer between Pd and H.<sup>[20]</sup>

To perform an electrochemical test, 7 nm Pd and PdH<sub>0.40</sub> NCs were supported on carbon black (Pd NCs/C and PdH<sub>0.40</sub> NCs/C). The CO<sub>2</sub>RR activity and selectivity of 7 nm Pd and PdH<sub>0.40</sub> NCs/C catalysts toward gaseous products were compared by the chronoamperometry (CA) test and gas chromatography (GC) quantification under the operating potential range between –0.5 and –1.0 V (Figure S5, Supporting Information). Figure 2a showed that the total Faradaic efficiencies (FEs) of CO (FE<sub>CO</sub>) and H<sub>2</sub> (FE<sub>H<sub>2</sub></sub>) were in the range of 88–100% for both samples, indicating that CO and H<sub>2</sub> were the major products. With increasing overpotential, the trends for the changes in FE<sub>H<sub>2</sub></sub> and FE<sub>CO</sub> were different. From –0.6 V, both electrocatalysts presented decreased FE<sub>CO</sub> and increased FE<sub>H<sub>2</sub></sub> toward higher potential, leading to reduced CO/H<sub>2</sub> ratios (Figure 2b). The decrease of FE<sub>CO</sub> could be ascribed to the limited CO<sub>2</sub> solubility during the CO<sub>2</sub>RR, thus incurring the mass transport limitation of reactant to the electrode surface, while for FE<sub>H<sub>2</sub></sub>, the reaction kinetics of HER was not limited by the diffusion of the proton donor in the aqueous electrolyte.

When comparing the CO<sub>2</sub>RR performance between Pd and PdH<sub>0.40</sub> NCs/C, the advantage of the prehydridized structure (PdH<sub>0.40</sub> NCs/C) was manifested by the tunable CO/H<sub>2</sub> ratios for syngas production with a significantly enhanced partial current density of CO. For example, at –0.6 V the CO/H<sub>2</sub> ratio obtained over Pd NCs/C was 0.95, which was increased to 1.68 over PdH<sub>0.40</sub> NCs/C. To obtain the syngas production with the

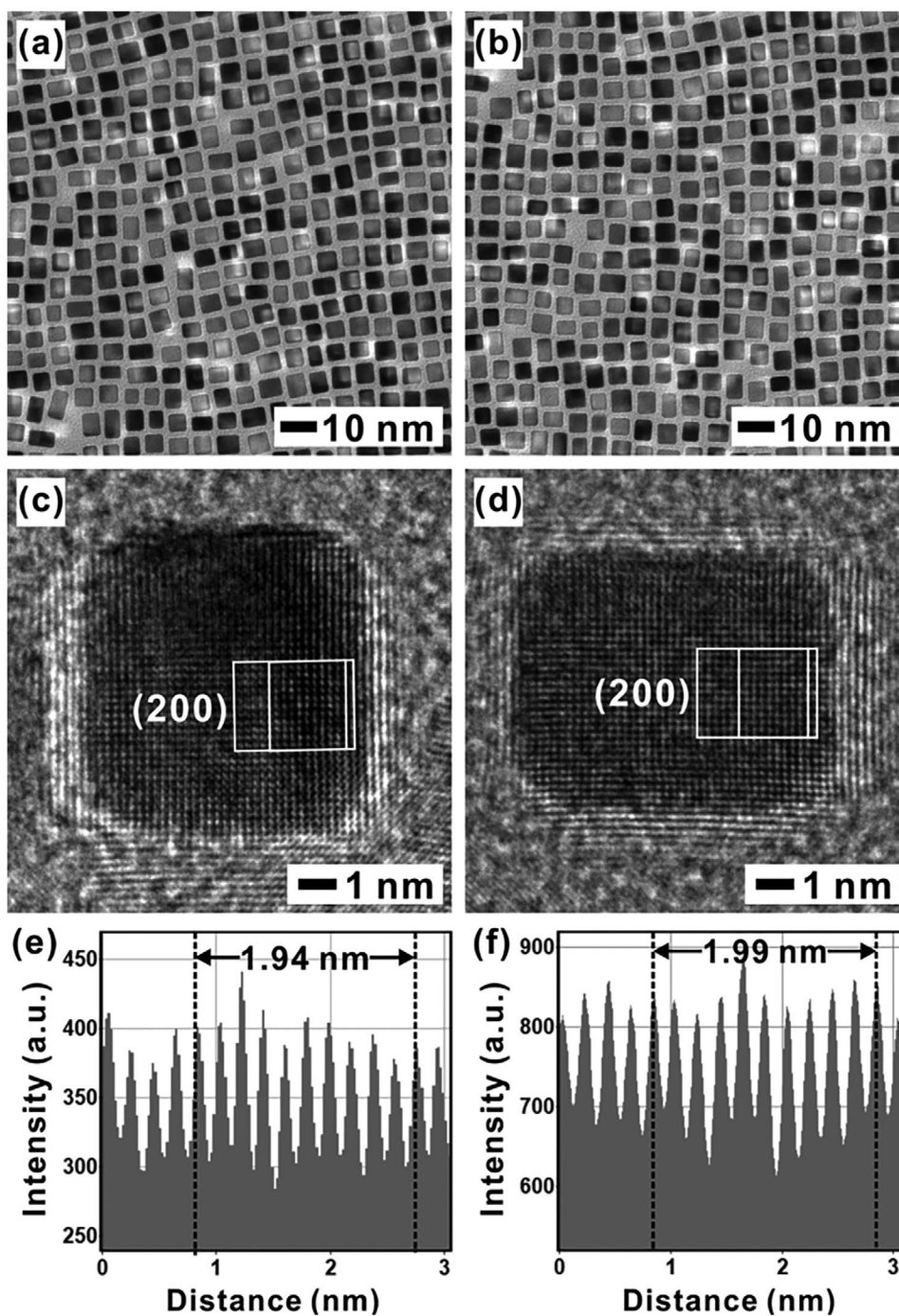


**Figure 1.** TEM images of a) Pd and b) PdH<sub>0.40</sub> NCs of 7 nm in nominal size. HRTEM images of c) a Pd and d) a PdH<sub>0.40</sub> NCs. Intensity profiles recorded from the area indicated by the rectangular box in HRTEM image for e) a Pd and f) a PdH<sub>0.40</sub> NC.

CO/H<sub>2</sub> ratio in the range of 1 to 2, the suitable potential for Pd NCs/C was allowed at  $-0.5$  V only, while for PdH<sub>0.40</sub> NCs/C, the potential range was extended from  $-0.5$  to  $-0.8$  V, making it more favorable to the syngas production from CO<sub>2</sub>RR. Moreover, the partial current density of CO ( $J_{CO}$ ) based on geometric electrode area of PdH<sub>0.40</sub> NCs/C also showed considerable enhancement compared with Pd NCs/C (Figure S6, Supporting Information). For instance, the  $J_{CO}$  of PdH<sub>0.40</sub> NCs/C was

2.6 times of the Pd counterparts at  $-0.6$  V. Considering the smaller electrochemical surface area (ECSA) of PdH<sub>0.40</sub> NCs/C due to the exposed surface \*H species (Figure S7, Supporting Information), the  $J_{CO}$  based on ECSA of Pd ( $j_{CO-Pd}$ ) of 7 nm PdH<sub>0.40</sub> was further increased by 2.2-fold compared with that of Pd NCs/C at  $-0.6$  V, suggesting a significantly improved CO<sub>2</sub>RR activity. Both Pd and PdH<sub>0.40</sub> NCs/C presented good stability at  $-0.7$  V (Figure S8, Supporting Information).

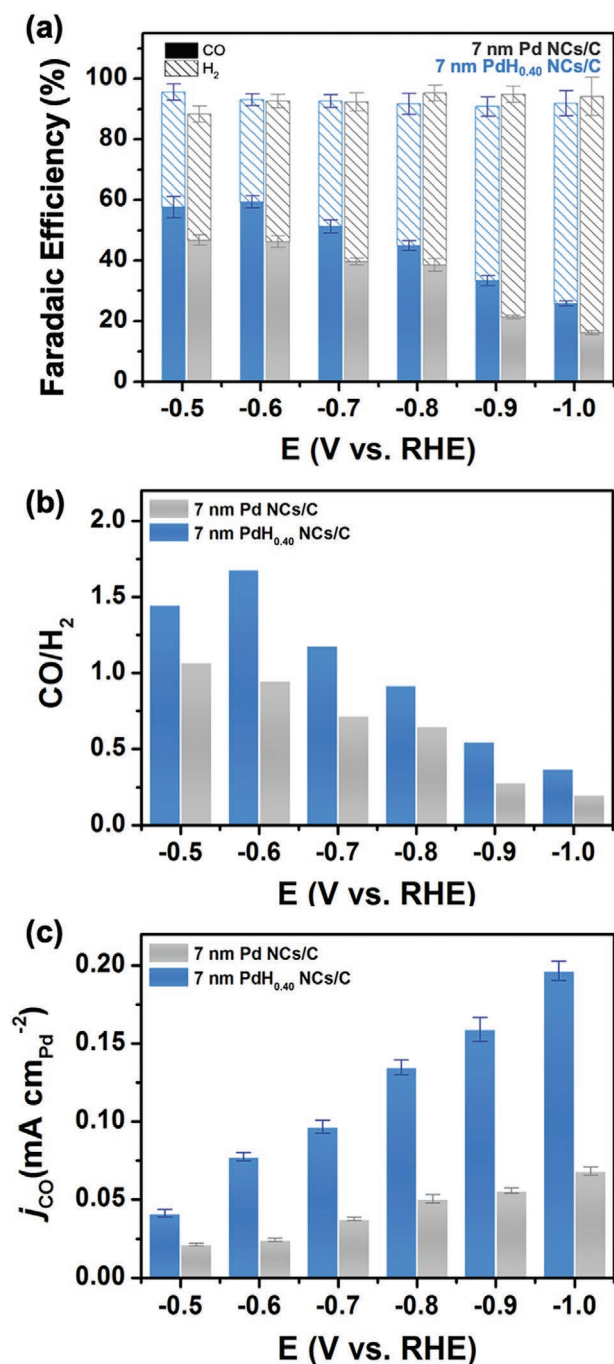


**Figure 2.** Electrocatalytic performance of 7 nm Pd and PdH<sub>0.40</sub> NCs/C from -0.5 to -1.0 V. a) Faradaic efficiency of CO and H<sub>2</sub>. b) CO/H<sub>2</sub> ratio. c) Partial current density of CO based on ECSA ( $j_{\text{CO-Pd}}$ ).

It is well-established that Pd can be readily transformed to PdH<sub>1</sub> at the electrochemical potentials for the CO<sub>2</sub>RR.<sup>[9]</sup> Accordingly, the active phase of both Pd and PdH<sub>0.40</sub> NCs/C in the CO<sub>2</sub>RR should be PdH<sub>1</sub> NCs. In that case, one should expect similar CO<sub>2</sub>RR performance for the Pd and PdH<sub>0.40</sub> NCs/C electrocatalysts. However, experimental results showed significantly different CO<sub>2</sub>RR performance, with PdH<sub>0.40</sub> NCs/C being far superior to Pd NCs/C.

Ex situ XAFS analysis was first performed to compare the chemical nature of Pd and PdH<sub>0.40</sub> NCs/C. Compared with Pd NCs/C, PdH<sub>0.40</sub> NCs/C showed negative shift of X-ray absorption near edge structure (XANES) profile and longer Pd–Pd bond distance from extended X-ray absorption fine structure (EXAFS) result, demonstrating the successful formation of Pd hydride (Figure S9 and Table S2, Supporting Information). In an attempt to monitor the change of the local chemical environment of Pd and PdH<sub>0.40</sub> NCs/C during the CO<sub>2</sub>RR, in situ XAFS analysis was then conducted (Figure 3) to investigate the origin of the enhanced CO<sub>2</sub>RR performance of PdH<sub>0.40</sub> NCs/C. Upon decreasing the potential for the electrochemical reduction from 0.6 V to -0.9 V, both Pd and PdH<sub>0.40</sub> NCs/C showed the gradual shift in the XANES profiles (Figure 3a,b) toward lower energy concurrently with an increase in the Pd–Pd interatomic distance as shown in the EXAFS profiles (Figure 3c–d, and Figure S10, Supporting Information). This can be attributed to the H uptake and consequent lattice expansion associated with the PdH<sub>1</sub> formation. However, the prehydrogenation process was found to play a role in the onset potential for the PdH<sub>1</sub> formation. The phase transition for Pd NCs/C took place at -0.7 V as evidenced by the shifts in both XANES and EXAFS profiles. For the PdH<sub>0.40</sub> NCs/C, this phase transition occurred at less cathodic potential of -0.3 V, indicating that the PdH<sub>0.40</sub> NCs more readily accepted the additional H compared to Pd NCs. The different H uptake manners could be more explicitly displayed in the change of the Pd–Pd interatomic distance for both catalysts as a function of applied potential (Figure 3e), illustrating the distinct electrochemical onset potentials toward the PdH<sub>1</sub> formation.

The facile transformation of PdH<sub>0.40</sub> to PdH<sub>1</sub> can be interpreted by several factors. One can speculate that the H uptake involved in the PdH formation entails an energy penalty related to (1) the mix of Pd and H orbitals, (2) the increase in the Pd–Pd distance, and (3) the resultant multiple H diffusion into the Pd lattice. Therefore, the prehydrogenation process should be efficient in mitigating the penalty by mixing the orbitals of Pd and H and increasing the Pd–Pd interatomic distance in advance, thus allowing the PdH formation to occur at a lower potential (reduced by 300 mV). This is further supported by the linear sweep voltammetry (LSV) curves (Figure S11, Supporting Information). Both catalysts showed the broad redox peaks associated with the PdH formation. Compared with Pd NCs/C, the peak in PdH<sub>0.40</sub> NCs/C was shifted positively by ≈40 mV. Furthermore, the earlier PdH<sub>1</sub> formation endowed PdH<sub>0.40</sub> with better tolerance against CO-poisoning, thus leading to a more rapid response of voltammetric current and an improved CO<sub>2</sub>RR activity of PdH<sub>0.40</sub> NCs/C after -0.8 V, even though both electrocatalysts presented the same stoichiometry of PdH<sub>1</sub>. The CO stripping experiment was conducted to investigate the CO anti-poisoning capability for both samples. (Figure S12, Supporting Information). Compared with Pd NCs/c, the main CO oxidation peak of PdH<sub>0.40</sub> NCs/C was negatively shifted by ≈20 mV, implying its enhanced CO anti-poisoning effect from the hydride structure. We also evaluated the CA of the PdH<sub>0.40</sub> in 0.1 M KOH solution at 1.2 V for 5 min and compared the phase and composition before and after the test using XRD (Figure S13, Supporting Information). The results showed no peak shift during CA test, indicating that PdH phase is stable under the whole CO-stripping potential.

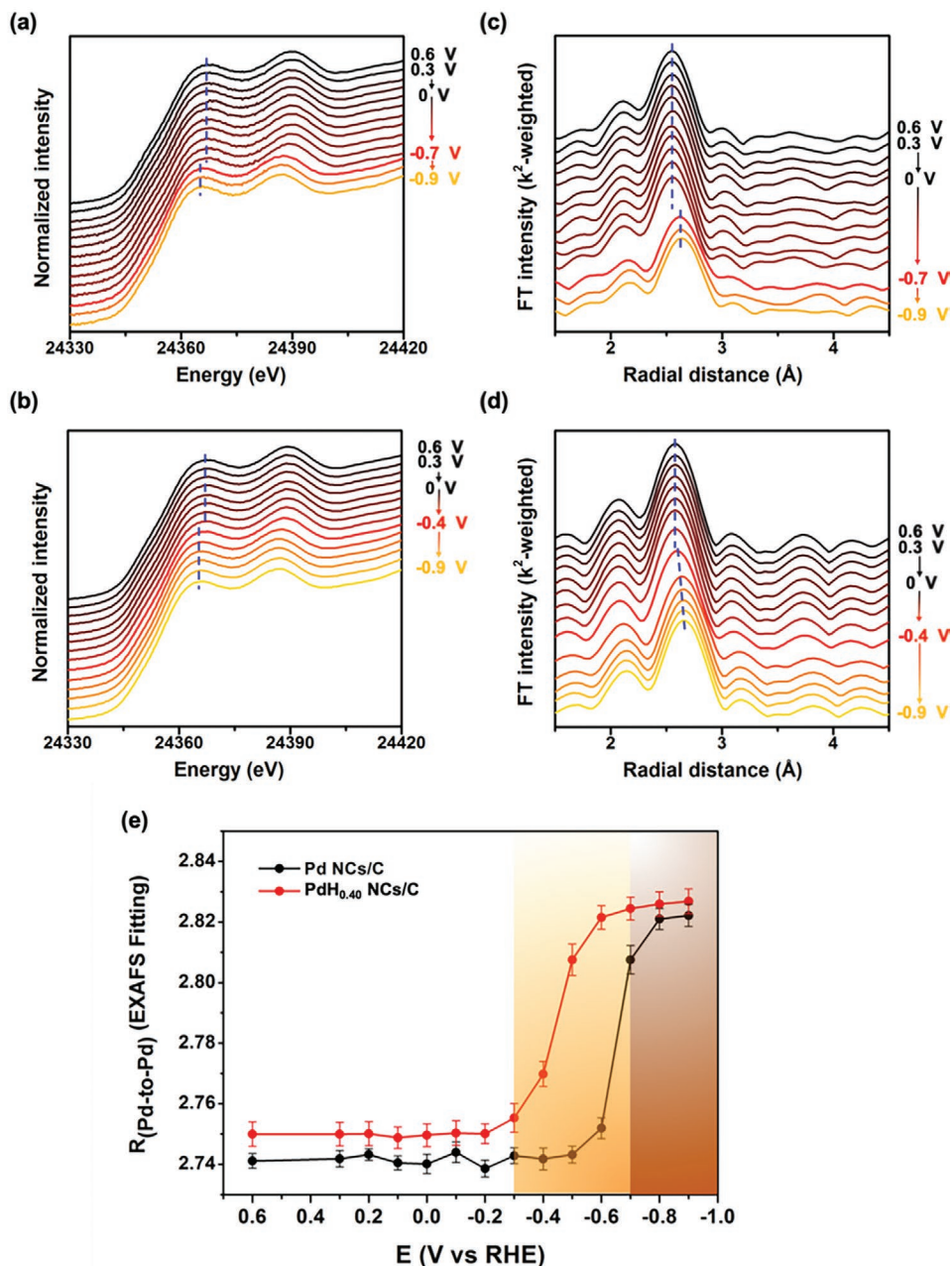


**Figure 3.** In situ XAFS profiles measured at Pd K-edge. Normalized XANES profiles for a) 7 nm Pd NCs/C and b) PdH<sub>0.40</sub> NCs/C. *k*<sup>2</sup>-weighted EXAFS spectra for c) 7 nm Pd NCs/C and d) PdH<sub>0.40</sub> NCs/C. e) The interatomic distance ( $R_{\text{Pd-Pd}}$ ) profiles for Pd and PdH<sub>0.40</sub> NCs/C as a function of applied potential determined from in situ EXAFS analysis.

It is observed that an optimal catalyst particle size exists in many catalytic reactions.<sup>[8,15]</sup> Thus, the size effect of Pd and PdH<sub>0.40</sub> NCs for CO<sub>2</sub>RR was also investigated. By adjusting the amount of KCl and KBr used for the synthesis of Pd NCs, 13 and 19 nm Pd NCs were obtained (Figures S14–S16, Supporting Information). These Pd NCs were also transformed to PdH<sub>0.40</sub> NCs under the same condition as that for 7 nm PdH<sub>0.40</sub> NCs (Figures S14–S16, Supporting Information). **Figure 4** shows that the beneficial role of the prehydrogenation process of the Pd NC catalysts in CO<sub>2</sub>RR was still valid regardless of the particle size. When the particle size increased to 13 and 19 nm,

all PdH<sub>0.40</sub> catalyst exhibited enhanced CO/H<sub>2</sub> ratios and  $J_{\text{CO}}$  compared with the corresponding Pd NCs of similar sizes (Figures S17 and S18, Supporting Information). The phenomenon of earlier PdH<sub>1</sub> peak formation from PdH<sub>0.40</sub> shown by LSV curves was also observed in 13 and 19 nm NCs (Figure S19, Supporting Information). Moreover, 13 and 19 nm PdH<sub>0.40</sub> NCs also presented improved tolerance against CO poisoning as shown from the negatively shifted CO oxidation peak in the CO stripping experiment (Figure S20, Supporting Information). It was noted that with increased particle size, the CO/H<sub>2</sub> ratios of Pd and PdH<sub>0.40</sub> NCs/C both decreased (Figure 4a,b), implying

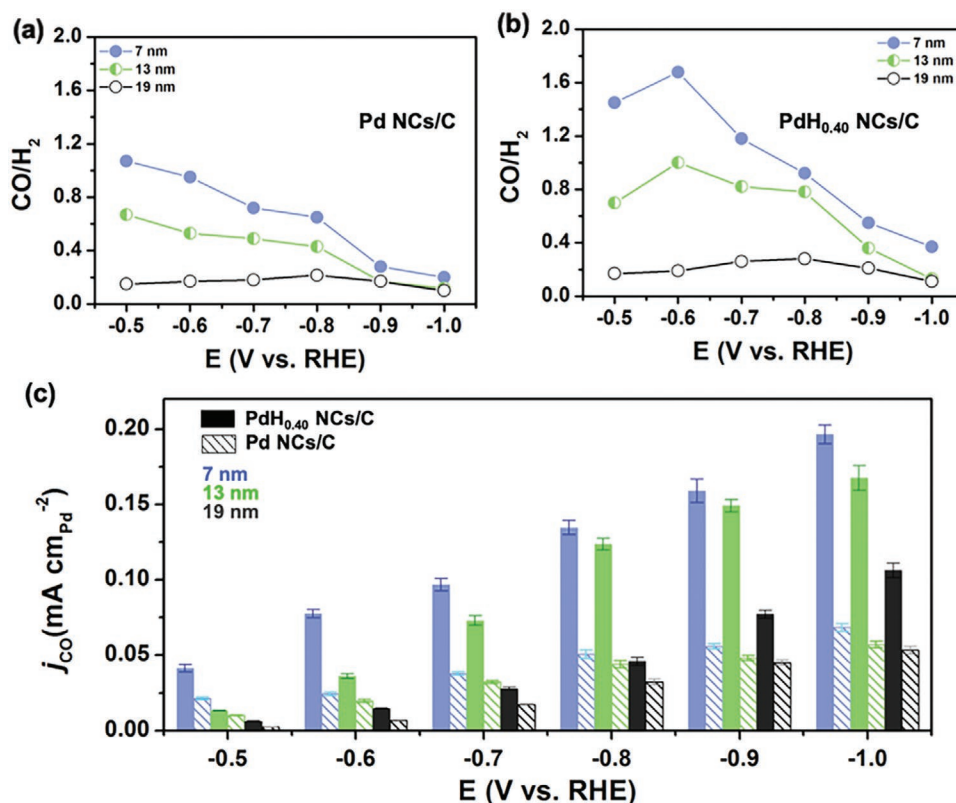


**Figure 4.** Size-dependent CO<sub>2</sub>RR performance from -0.5 to 1.0 V. CO/H<sub>2</sub> ratios obtained from a) Pd NCs b) PdH<sub>0.40</sub> NCs. c) Partial current density of CO based on ECSA ( $j_{\text{CO-Pd}}$ ) of all the prepared electrocatalysts.

a hindered CO<sub>2</sub>RR rate for the large NCs. Due to the different ECSAs of Pd and PdH<sub>0.40</sub> NCs/C, the  $j_{\text{CO-Pd}}$  of all samples was also compared and showed the similar trends for both Pd and PdH<sub>0.40</sub> NCs: 7 nm > 13 nm > 19 nm (Figure S21 and Table S3, Supporting Information).

The above results suggest that in addition to the contribution of the hydride structure, the CO<sub>2</sub>RR activity and selectivity of Pd NC catalysts also strongly depend on the particle size. The smaller NC size, the higher CO<sub>2</sub>RR activity, and selectivity towards CO production, which can be also supported by a previous study on demonstrating the different active sites (edge, corner, and terrace sites) of Pd for CO<sub>2</sub>RR and HER.<sup>[15]</sup> For CO<sub>2</sub>RR, the adsorption of CO<sub>2</sub> and the formation of key reaction intermediate \*HOCO are more preferable to the edge and corner sites, while for HER, the formation of H\* remains similar on all three types of sites. As the smaller NCs size leads to more abundant active sites (edge and corner sites), the CO<sub>2</sub>RR performance in terms of CO production can be significantly improved. In addition, the enhancement factor from the pre-hydridization effect also decreased with the increased size. For example, at -0.8 V, 7 nm PdH<sub>0.40</sub> NCs/C presented  $\approx 160\%$  increased  $j_{\text{CO-Pd}}$  relative to the Pd counterpart. While for 19 nm PdH<sub>0.40</sub> NCs/C, it only showed  $\approx 44\%$  improvement compared to the corresponding Pd NCs/C. The possible reason might be that the prehydridization effect is also correlated to different sites, which might be more significant on the edge and corner sites than the terrace ones.

DFT calculations were performed to determine the lattice parameter of PdH<sub>x</sub> with various H concentrations ( $x = 0-100\%$ ). In agreement with the experimental measurements, the DFT results (Table S5, Supporting Information) predicted that the lattice parameter and Pd-Pd bond length increased with increasing H content in the PdH<sub>x</sub> bulk structures. Additional DFT calculations were carried out to obtain the binding energies of intermediates of CO<sub>2</sub>RR (i. e. \*CO and \*HOCO) and HER (i. e. \*H) on Pd(100), PdH<sub>0.5</sub>(100), and PdH<sub>1</sub>(100) surfaces (Table S6, Supporting Information). A PdH<sub>0.5</sub>(100) surface generated using a bulk PdH<sub>0.5</sub> structure, computationally much simpler to model compared to the PdH<sub>0.4</sub> phase, was modeled to represent the surface of PdH<sub>0.4</sub> nanocubes.

The DFT calculated binding energies of the intermediates in their most favorable sites (shown in Figure 5a-d and listed in Table S6, Supporting Information) revealed a weakened binding on PdH<sub>x</sub>(100) compared to Pd(100). Free energy diagrams were constructed using the DFT calculated binding energies in Table S6, Supporting Information. The calculated free energy diagrams (Figure 5e-f) showed a thermodynamically favorable formation of the HER and CO<sub>2</sub>RR intermediates on Pd(100). However, the CO<sub>2</sub>RR activity on Pd(100) should be limited by a large desorption barrier of \*CO (i. e. \*CO + H<sub>2</sub>O(g)  $\rightarrow$  CO(g) + H<sub>2</sub>O(g) + \*) due to a strong binding affinity of Pd(100) for the CO intermediate. In contrast, as shown in Figure 5e-f, the weakened binding of adsorbates resulted in the formation of the \*H intermediate for HER and \*HOCO for CO<sub>2</sub>RR

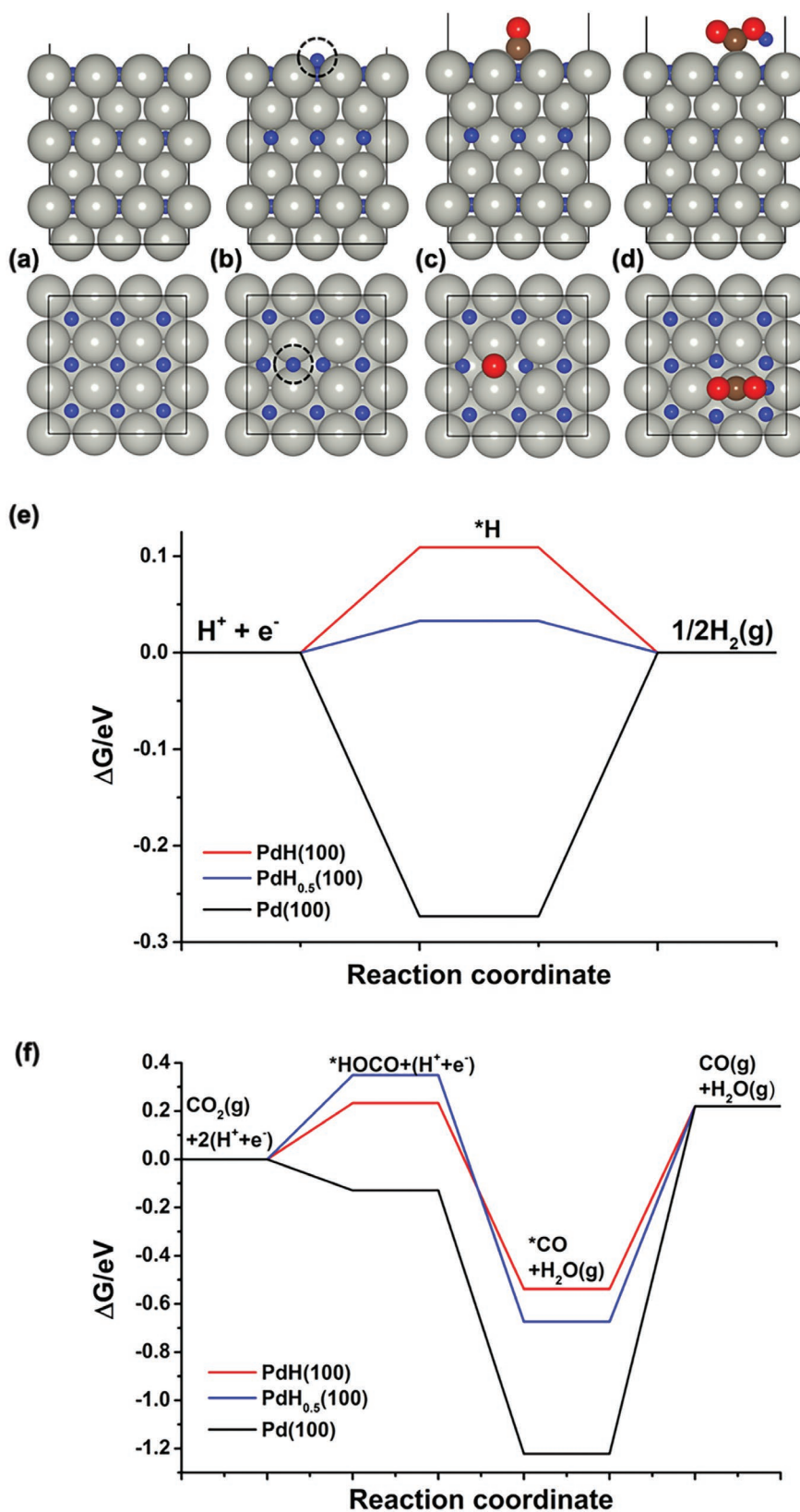


**Figure 5.** DFT optimized structures of a) PdH<sub>0.5</sub>(100) surface, b) \*H, c) \*CO, and d) \*HOCO adsorbed at the most favorable site on PdH<sub>0.5</sub>(100). Black solid lines show the unit cell used in the DFT calculations and the dotted circle shows the adsorbed \*H atom on PdH<sub>0.5</sub>(100). Pd: gray, H: blue, O: red, and C: brown. DFT calculated free energy diagrams of e) HER, and f) CO<sub>2</sub>RR on Pd(100), PdH(100), and PdH<sub>0.5</sub>(100) surfaces at a potential ( $U$ ) = 0 V.

being uphill on PdH<sub>0.5</sub>(100) and PdH(100). It was noticed that relatively small applied external potential should be sufficient to make the formation of \*H and \*HOCO downhill in energy. Furthermore, the weaker binding of \*CO made the overall CO<sub>2</sub>RR favorable on PdH<sub>x</sub>(100) surfaces. Thus, in line with the experimental findings, DFT results indicated that the formation of PdH<sub>x</sub> should enhance the CO<sub>2</sub>RR compared to Pd.

### 3. Conclusions

In summary, combined results from electrochemical measurements, in situ XAFS characterization, and DFT calculations show the benefit of prehydride PdH<sub>0.40</sub> NC over the Pd counterpart for the syngas production from the CO<sub>2</sub>RR. Under the CO<sub>2</sub>RR conditions, both of the PdH<sub>0.40</sub> and Pd NCs would be transformed into the stoichiometric PdH<sub>1</sub>. Nevertheless, compared with Pd NCs/C, PdH<sub>0.40</sub> NCs/C presented less cathodic phase transformation (to PdH<sub>1</sub>) by 300 mV, leading to an enhanced CO<sub>2</sub>RR performance of PdH<sub>0.40</sub> NCs/C. The CO/H<sub>2</sub> ratios and CO<sub>2</sub>RR activity of 7 nm PdH<sub>0.40</sub> NCs/C were significantly improved compared with that of Pd NCs/C with the similar size at the low overpotential (i.e., -0.6 V), respectively. Also, PdH<sub>0.40</sub> NCs/C showed extended suitable potential range for syngas production (CO/H<sub>2</sub> ratios between 1 and 2) in comparison with Pd NCs/C. We also discovered that the size effect also played a key role in determining the CO<sub>2</sub>RR performance, with smaller NC size showing higher activity. These results suggest strategies to design more active and selective electrocatalysts for CO<sub>2</sub>RR with tunable product compositions.

### 4. Experimental Section

**Size-Controlled Synthesis of Pd NCs (Size of 7, 13, and 19 nm):** To control the size of Pd NCs, the amounts of KCl and KBr were varied.<sup>[25]</sup> The reaction mixture including 60 mg of AA, 105 mg of PVP (Mw ≈ 55 000), different amount of KCl (150 mg for 7 nm and no addition for 13 and 19 nm in nominal size), different amount of KBr (5, 300, and 600 mg for 7, 13, and 19 nm in nominal size, respectively) and 8 mL of DI water was placed in a 25 mL glass vial, which was pre-heated at 80 °C for 10 min in an oil bath under magnetic stirring. Then, 3 mL of DI water containing 57 mg of Na<sub>2</sub>PdCl<sub>4</sub> was added into the pre-heated mixture. The vial was maintained at 80 °C for 3 h. The final product was collected by centrifugation at 12000 rpm for 10 min. The resulting Pd NCs were re-dispersed in ethanol or DMF.

**Conversion of Pd NCs into Pd Hydride NCs (PdH<sub>0.40</sub> NCs):** After centrifugation of Pd NCs, they were dispersed in 30 mL of DMF (0.67 mg<sub>Pd</sub> mL<sup>-1</sup>) solution containing 30 mg of PVP. The reaction mixture was heated at 160 °C for 16 h in an oil bath under magnetic stirring. The final product was collected by centrifugation at 12000 rpm for 10 min. The resulting PdH<sub>0.40</sub> NCs were re-dispersed in ethanol.<sup>[20]</sup>

**Preparation of Pd NCs or PdH<sub>0.40</sub> NCs Catalysts by Carbon Loading:** Suspension of 20 mg Pd NCs or PdH<sub>0.40</sub> NCs and 80 mg of Vulcan XC-72 carbon black were dispersed in 15 mL of ethanol. Then the mixture was sonicated for 2 h and the product was collected by centrifugation. Each catalyst was washed five times with ethanol and dried by Argon (Ar) gas.

**Material Characterization:** Transmission electron microscopy (TEM) images were taken using an HT-7700 microscope (HITACHI, Japan) operated at 100 kV by drop-casting the nanoparticle dispersions on carbon-coated copper grids and drying under ambient conditions. High-resolution TEM studies were carried out in a Titan G2 ChemiSTEM Cs Probe microscope (FEI, USA) operated at 200 kV. X-ray diffraction (XRD) patterns

were collected with X-ray diffractometer (PANalytical X'pert PRO-MPD/MRD) using a Cu-K $\alpha$  radiation at 40 kV and 25 mA. TEM and XRD instruments were conducted at Korea Basic Science Institute (KBSI, Daegu Korea). XPS was measured through Scientific ESCALAB 250Xi system (ThermoFisher) with Al K $\alpha$  X-ray (1486.6 eV) as the light source, which was conducted at National NanoFab Center (NNFC, Daejeon, Korea). Metal contents in nanocrystals were determined by inductively coupled plasma-atomic emission spectrometry (ICP-AES, Perkin-Elmer, Optima 7300DV).

**Electrochemical Measurements:** The air-tight H-cell was used for the electrochemical measurement. The 0.5M sodium bicarbonate (NaHCO<sub>3</sub>) solution prepared from CO<sub>2</sub>-saturated 0.25M sodium carbonate (Na<sub>2</sub>CO<sub>3</sub>) solution was utilized as an electrolyte. The catalyst ink was prepared by dispersing 2.5 mg of electrocatalysts in a mixture solution containing 2.0 ml of Milli-Q water, 0.5 ml of isopropanol, 10  $\mu$ l of Nafion (5%), and then 100  $\mu$ l of each catalyst ink was deposited on a working electrode (carbon paper: Toray carbon paper 060). The graphite paper and Ag/AgCl (3M Cl<sup>-</sup>) were used as the counter and reference electrode, respectively. The potentials were calibrated to a reversible hydrogen electrode (RHE). During the test, the electrolyte was vigorously stirred to mitigate the mass transport limitation of dissolved CO<sub>2</sub>. To obtain stable electrochemical CO<sub>2</sub> reduction data, the working electrode was first held at -0.05 V for 60 s to remove the capping agents (PVP, Br<sup>-</sup>) of electrocatalysts and then cycled in 0.02–0.8 V for three times at 50 mV s<sup>-1</sup>. After purging CO<sub>2</sub> for additional 10 min, the CA test was used to evaluate the CO<sub>2</sub>RR performance of electrocatalysts by holding each potential (from -0.5 to -1.0 V) for a designated duration. After finishing the CA test at specified potential, 100  $\mu$ l of gas in the empty head space ( $\approx$ 17 ml) of cathodic compartment was injected into gas chromatography (GC, S46 Agilent, Agilent 7890B) to obtain the gaseous product distribution. The CO stripping experiment was performed to obtain the CO anti-poisoning capability of electrocatalysts. The CO adsorption was achieved by holding the pre-cleaned electrode potential at 0.05 V for 10 min in a CO-saturated 0.1 M KOH. The excess CO was cleared by purging Ar for 30 min. The CO stripping curves were then taken with a scanning rate of 50 mV s<sup>-1</sup>. The Cu underpotential deposition (Cu UPD) was conducted in an Ar-saturated 50 mM H<sub>2</sub>SO<sub>4</sub> + 50 mM CuSO<sub>4</sub> solution at 10 mV s<sup>-1</sup>. See Supporting Information for the details about the calculation methods.

**In Situ XAFS Measurements:** A lab-made acrylic kit was used for the in situ XAFS measurement. The areal mass loading of the working electrode was  $\approx$ 5 mg cm<sup>-2</sup> to achieve sufficient XAFS signal. During the measurements, CO<sub>2</sub> gas was continuously bubbled into the electrolyte. The hydrogen electrode (Hydroflex, E-DAQ) was used as a reference electrode. The other electrochemical conditions were the same as in the electrochemical measurements. In situ XAFS measurements were conducted on the 7-BM (QAS) beamline in National Synchrotron Light Source-II (NSLS-II) at Brookhaven National Laboratory. The XAFS signal was recorded with a fluorescence mode using a Canberra PIPS detector. The electrocatalytic performance was measured by stepwise potential sweeping from 0.6 to -0.9 V. Each potential was held for 10 min using chronoamperometry technique during the XAFS measurement. The typical duration for a single spectrum was  $\approx$ 45 sec and the last ten spectra measured at each potential were merged to get high signal-to-noise spectrum. During the measurements, the reference spectrum of Pd foil was recorded at the same time, and was further used in calibrating the edge energy ( $E_0$ ) of the samples under analysis.

The obtained spectra were processed using the ATHENA and ARTEMIS software in IFFEFIT package.<sup>[26–28]</sup> EXAFS analyses were conducted by using the ARTEMIS software. The EXAFS spectrum ( $\chi(k)$ ) was weighted with  $k^2$  value to intensify the signal in the high  $k$ -regime. The Hanning window was utilized for the Fourier-transform. All of the EXAFS fittings were done in the R-space. The goodness of fitting was evaluated based on the reliable factor ( $R$ -factor) and reduced chi-square (reduced  $\chi^2$ ). The amplitude reduction factor for Pd was obtained from the reference Pd foil. For the EXAFS fitting, FCC Pd ( $a = 3.900$  Å) model was used. All of the data were co-refined using this model. A single-scattering path between Pd and its first neighbor Pd was taken into consideration for all EXAFS fitting. The fitting results were tabulated in Table S4, Supporting Information.

**Computational Methods:** Periodic DFT<sup>[29–30]</sup> calculations were performed using the plane wave Vienna Ab Initio Simulation Package (VASP) code.<sup>[31–32]</sup> The core electrons were described using the projector augmented wave (PAW) potentials with the generalized gradient approximation (GGA),<sup>[33–34]</sup> using PW91 functionals.<sup>[35]</sup> A plane-wave basis set with a kinetic energy cutoff of 400 eV was used in all calculations. The Brillouin zone integration was performed using a  $3 \times 3 \times 1$  Monkhorst-Pack grid.<sup>[36]</sup>

The Pd(100) surface was modeled using a six-layer  $3 \times 3$  surface slab. Similarly, the H-terminated PdH(100) and PdH<sub>0.5</sub>(100) surfaces were modeled using six-layer  $3 \times 3$  surface slabs using the NaCl crystal structure for bulk PdH and PdH<sub>0.5</sub> (with 50% fewer H atoms compared to bulk PdH), respectively. A vacuum layer of  $\approx 14$  Å thick was added in the slab cell along the direction perpendicular to the surface to minimize the artificial interactions between the surface and its periodic images. During geometry optimization, atoms in the top three layers were allowed to relax while atoms in the bottom three layers were fixed until the Hellman–Feynman force on each ion was smaller than  $0.01$  eV Å<sup>-1</sup>. The binding energy (BE) of adsorbate was calculated as:

$$BE(\text{adsorbate}) = E(\text{slab} + \text{adsorbate}) - E(\text{slab}) - E(\text{adsorbate}) \quad (1)$$

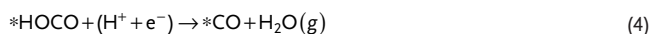
where  $E(\text{slab} + \text{adsorbate})$ ,  $E(\text{slab})$ , and  $E(\text{adsorbate})$  were the total energy of slab with adsorbate, clean slab, and adsorbate in the gas phase, respectively.  $E(\text{H})$  was taken as one-half of the total energy of the H<sub>2</sub> molecule during the calculation of hydrogen BE.

The Gibbs free energy ( $G$ ) was calculated as<sup>[37]</sup>

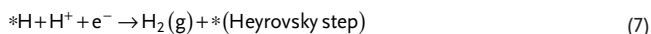
$$G = E + ZPE - TS \quad (2)$$

Here,  $E$  was the total energy obtained from DFT calculations, ZPE and  $S$  were the zero-point energy and entropy respectively, and  $T = 298.15$  K.

The free energy diagram of CO<sub>2</sub>RR to CO has been calculated by considering the following sequential steps:<sup>[8]</sup>



In aqueous electrolytes, the HER inevitably takes place via the following sequential steps,<sup>[10]</sup> and competes with the CO<sub>2</sub>RR:



## Supporting Information

Supporting Information is available from the Wiley Online Library or from the author.

## Acknowledgements

Q.C., J.K., and J.H.L. contributed equally to this work. Z.C. and Q.C. acknowledge the support from the ACS Petroleum Research Fund (#59989-DNI5) and Jacob School of Engineering at UC San Diego. S.-I.C. and J.K. acknowledge support by the National Research Foundation of Korea (NRF-2018R1C1B6004272, 2009-0082580). Authors at Columbia University acknowledge support by the U.S. Department of Energy, Office of Science, Catalysis Science Program (DE-FG02-13ER16381). This research used resources at 7-BM (QAS) of the National Synchrotron Light Source II, a U.S. Department of Energy (DOE) Office of Science User

Facility operated for the DOE Office of Science by Brookhaven National Laboratory under Contract No. DE-SC0012704 with assistance from the Synchrotron Catalysis Consortium (DE-SC0012653). The DFT calculations were performed using computational resources at the Extreme Science and Engineering Discovery Environment (TGCH190032), which is supported by National Science Foundation Grant number ACI-1548562 and at the National Energy Research Scientific Computing Center (NERSC), a U.S. Department of Energy Office of Science User Facility operated under Contract No. DE-AC02-05CH11231.

## Conflict of Interest

The authors declare no conflict of interest.

## Keywords

carbon dioxide reduction reaction (CO<sub>2</sub>RR), density functional theory (DFT), nanocubes, palladium hydride (PdH<sub>1</sub>), syngas

Received: August 28, 2020

Revised: October 18, 2020

Published online:

- [1] M. Meinshausen, N. Meinshausen, W. Hare, S. C. Raper, K. Frieler, R. Knutti, D. J. Frame, M. R. Allen, *Nature* **2009**, 458, 1158.
- [2] C. Long, X. Li, J. Guo, Y. Shi, S. Liu, Z. Tang, *Small Methods* **2019**, 3, 1800369.
- [3] M. Gattrell, N. Gupta, A. Co, *J. Electroanal. Chem.* **2006**, 594, 1.
- [4] Y. i. Hori, in *Modern aspects of electrochemistry*, Springer, New York **2008**, p 89.
- [5] B. M. Tackett, E. Gomez, J. G. Chen, *Nat. Catal.* **2019**, 2, 381.
- [6] Y. Pan, R. Lin, Y. Chen, S. Liu, W. Zhu, X. Cao, W. Chen, K. Wu, W.-C. Cheong, Y. Wang, *J. Am. Chem. Soc.* **2018**, 140, 4218.
- [7] S. Liu, H. Tao, L. Zeng, Q. Liu, Z. Xu, Q. Liu, J.-L. Luo, *J. Am. Chem. Soc.* **2017**, 139, 2160.
- [8] W. Zhu, R. Michalsky, O. n. Metin, H. Lv, S. Guo, C. J. Wright, X. Sun, A. A. Peterson, S. Sun, *J. Am. Chem. Soc.* **2013**, 135, 16833.
- [9] W. Sheng, S. Kattel, S. Yao, B. Yan, Z. Liang, C. J. Hawxhurst, Q. Wu, J. G. Chen, *Energy Environ. Sci.* **2017**, 10, 1180.
- [10] Q. Lu, J. Rosen, Y. Zhou, G. S. Hutchings, Y. C. Kimmel, J. G. Chen, F. Jiao, *Nat. Commun.* **2014**, 5, 3242.
- [11] J. Wang, S. Kattel, C. J. Hawxhurst, J. H. Lee, B. M. Tackett, K. Chang, N. Rui, C. J. Liu, J. G. Chen, *Angew. Chem.* **2019**, 58, 6271.
- [12] I. Wender, *Fuel Process. Technol.* **1996**, 48, 189.
- [13] J. H. Lee, S. Kattel, Z. Jiang, Z. Xie, S. Yao, B. M. Tackett, W. Xu, N. S. Marinkovic, J. G. Chen, *Nat. Commun.* **2019**, 10, 3724.
- [14] Y. Hori, H. Wakebe, T. Tsukamoto, O. Koga, *Electrochim. Acta* **1994**, 39, 1833.
- [15] D. Gao, H. Zhou, J. Wang, S. Miao, F. Yang, G. Wang, J. Wang, X. Bao, *J. Am. Chem. Soc.* **2015**, 137, 4288.
- [16] W. Zhu, S. Kattel, F. Jiao, J. G. Chen, *Adv. Energy Mater.* **2019**, 9, 1802840.
- [17] H. Huang, H. Jia, Z. Liu, P. Gao, J. Zhao, Z. Luo, J. Yang, J. Zeng, *Angew. Chem.* **2017**, 56, 3594.
- [18] J. K. Nørskov, F. Abild-Pedersen, F. Studt, T. Bligaard, *Proc. Natl. Acad. Sci. U. S. A.* **2011**, 108, 937.
- [19] Y. Liu, D. Tian, A. N. Biswas, Z. Xie, S. Hwang, J. H. Lee, H. Meng, J. G. Chen, *Angew. Chem.* **2020**, 59, 11345.
- [20] M. K. Kabiraz, J. Kim, W.-J. Lee, B. Ruqia, H. C. Kim, S.-U. Lee, J.-R. Kim, S.-M. Paek, J. W. Hong, S.-I. Choi, *Chem. Mater.* **2019**, 31, 5663.
- [21] J. Eastman, L. Thompson, B. Kestel, *Phys. Rev. B* **1993**, 48, 84.

- [22] Z. Zhao, X. Huang, M. Li, G. Wang, C. Lee, E. Zhu, X. Duan, Y. Huang, *J. Am. Chem. Soc.* **2015**, *137*, 15672.
- [23] P. Bennett, J. Fuggle, *Phys. Rev. B* **1982**, *26*, 6030.
- [24] C. T. Chan, S. G. Louie, *Phys. Rev. B* **1983**, *27*, 3325.
- [25] M. Liu, Y. Zheng, L. Zhang, L. Guo, Y. Xia, *J. Am. Chem. Soc.* **2013**, *135*, 11752.
- [26] S. Kelly, D. Hesterberg, B. Ravel, *Methods of Soil Analysis Part 5—Mineralogical Methods* **2008**, *5*, 387.
- [27] B. Ravel, M. Newville, *J. Synchrotron Rad.* **2005**, *12*, 537.
- [28] J. J. Rehr, R. C. Albers, *Rev. Mod. Phys.* **2000**, *72*, 621.
- [29] P. Hohenberg, W. Kohn, *Phys. Rev.* **1964**, *136*, B864.
- [30] W. Kohn, L. J. Sham, *Phys. Rev.* **1965**, *140*, A1133.
- [31] G. Kresse, J. Furthmüller, *Comput. Mater. Sci.* **1996**, *6*, 15.
- [32] G. Kresse, J. Hafner, *Phys. Rev. B* **1993**, *48*, 13115.
- [33] G. Kresse, D. Joubert, *Phys. Rev. B* **1999**, *59*, 1758.
- [34] P. E. Blöchl, *Phys. Rev. B* **1994**, *50*, 17953.
- [35] J. P. Perdew, Y. Wang, *Phys. Rev. B* **1992**, *45*, 13244.
- [36] H. J. Monkhorst, J. D. Pack, *Phys. Rev. B* **1976**, *13*, 5188.
- [37] J. K. Nørskov, J. Rossmeisl, A. Logadottir, L. Lindqvist, J. R. Kitchin, T. Bligaard, H. Jonsson, *J. Phys. Chem. B* **2004**, *108*, 17886.